

A three generation oscillation analysis of the Super-Kamiokande atmospheric neutrino data beyond one mass scale dominance approximation

*Sandhya Choubey*¹, *Srubabati Goswami*², *Kamales Kar*³

Saha Institute of Nuclear Physics,

1/AF, Bidhannagar, Calcutta 700064, INDIA.

Abstract

In this paper we do a three-generation oscillation analysis of the latest (848 days) Super-Kamiokande (SK) atmospheric neutrino data going beyond the one mass scale dominance (OMSD) approximation. We fix $\Delta_{12} = \Delta_{13}$ (Δ_{LSND}) in the range 0.5 - 2 eV² as allowed by the results from LSND and other accelerator and reactor experiments on neutrino oscillation and keep Δ_{23} (Δ_{ATM}) and the three mixing angles as free parameters. In such a scenario, the oscillation probabilities for the accelerator and reactor neutrinos involve only two of the mixing angles θ_{12} and θ_{13} and one mass scale. But the atmospheric neutrino oscillation is in general governed by both mass scales and all the three mixing angles. The higher mass scale gives rise to Δm^2 independent average oscillations for atmospheric neutrinos and does not enter the χ^2 analysis as an independent parameter. The Δ_{23} and the three mixing angles on the other hand appear as independent parameters in the χ^2 analysis and the best-fit values of these are determined from an analysis of a) the SK data, b) the SK and CHOOZ data. The allowed values of the mixing angles θ_{12} and θ_{13} from the above analysis are compared with the constraints from LSND and other accelerator and reactor experiments. Implications for future long baseline experiments are discussed.

¹sandhya@tnp.saha.ernet.in

²sruba@tnp.saha.ernet.in

³kamales@tnp.saha.ernet.in

1 Introduction

The Super-Kamiokande results on atmospheric neutrino flux measurement show a deficit of the ν_μ flux [1]. Two generation analyses of the SK data show that the $\nu_\mu - \nu_\tau$ or $\nu_\mu - \nu_s$ oscillation hypothesis provide a better fit to the SK data than the $\nu_\mu - \nu_e$ oscillation [2, 3, 4]. The high statistics of SK also makes it possible to study the zenith-angle dependence of the neutrino flux from which one can conclude that the ν_μ 's show signs of oscillation but the ν_e events are consistent with the no-oscillation hypothesis. Independently the results from the reactor experiment CHOOZ [5] disfavours the $\nu_\mu - \nu_e$ oscillation hypothesis in a two-generation analysis. It is important however to see the implications of these results in a three-generation picture. The most popular three-generation picture in the context of the SK data is the scenario shown in fig. 1a, where one of the mass squared differences is in the solar neutrino range and the other is suitable for atmospheric neutrino oscillations [4, 6]. In such a scheme one mass scale dominance applies for atmospheric neutrinos and the relevant probabilities are functions of two of the mixing angles and one mass squared difference. This picture however cannot explain the LSND results [7]. In this paper we perform a three flavor χ^2 -analysis of the SK atmospheric neutrino data assuming a mass pattern with $\Delta_{12} \simeq \Delta_{13}$ fixed in the range $0.5 - 2 \text{ eV}^2$ and allowing the other mass scale to vary between $10^{-4} \text{ eV}^2 \leq \Delta_{23} \leq 10^{-1} \text{ eV}^2$. This mass pattern is shown in fig. 1b. Apart from being suitable to explain the SK atmospheric neutrino data this spectrum is also interesting for the laboratory based neutrino oscillation experiments as the higher mass scale is explorable in the short base line experiments, whereas the lower mass scale can be probed in the long base line experiments. In this scheme to a good approximation, neutrino oscillation in the short-base line accelerators and reactors will be governed by one (the higher) mass scale [8, 9] – and only two of the mixing angles appear in the expressions for the oscillation probabilities. For the atmospheric and the long baseline experiments the characteristic energy and length scales are such that in general both mass differences are of relevance and the probabilities involve all the three mixing angles. However the higher mass scale gives rise to Δm^2 independent average oscillations

and it does not enter the χ^2 fit directly. We determine the best-fit values of Δ_{23} and the three mixing angles by performing a χ^2 analysis of

- the SK atmospheric neutrino data
- SK atmospheric and CHOOZ data

Finally we compare the allowed values of the mixing angles as obtained from the above analysis with those allowed by the other accelerator and reactor neutrino oscillation data including LSND.

The mass scheme of this paper was first considered in [10, 11] after the declaration of the LSND result. These papers performed a combined three generation analysis of accelerator and reactor results as well as the Kamiokande atmospheric neutrino data. Three-generation picture with the higher mass difference in the eV^2 range and the lower mass difference in the atmospheric range has also been considered in [12, 13] (pre-SK) and [14, 15, 16, 17] (post-SK). However these papers sought an explanation for all the three anomalies – namely the solar neutrino puzzle, the atmospheric neutrino problem as well as the LSND result within this three flavour picture. They attempted to explain both solar and atmospheric neutrino anomalies mainly by maximal $\nu_\mu \leftrightarrow \nu_e$ oscillations driven by $\Delta_{ATM} \sim 10^{-3} \text{ eV}^2$. Although it was claimed in [14, 15] that this scenario can provide a good fit to all the available data on neutrino oscillations, it was shown in [16] and also later in [17] that this scenario cannot reproduce the zenith angle dependence of the SK atmospheric neutrino data.

Our point of view is different. We do not attempt to solve the solar neutrino problem with this mass spectrum as it gives energy independent suppression of solar neutrino flux, which is shown to be ruled out at 99% C.L. [18] by the solar neutrino data. *Our aim is to determine the allowed oscillation parameter ranges consistent with SK atmospheric, CHOOZ, LSND and other accelerator and reactor experiments.*

A simultaneous solution of the solar neutrino problem as well would then call for the introduction of a light sterile neutrino which opens up many possibilities. Detailed analysis shows that complete hierarchy of four neutrinos ($m_1 \ll m_2 \ll m_3 \ll m_4$)

is not favoured by current data [19]. Mass patterns with three neutrino states closely degenerate in mass and the fourth one separated from these by the LSND gap is also not preferred. The allowed spectra seem to be the one in which two degenerate mass states are separated by the LSND gap [19, 20, 21]. The three generation scheme considered by us can be extended to include an extra sterile neutrino to take care of the solar neutrino data. However the three-generation scheme, in which one mass squared difference is in the solar range and the other in the atmospheric range, does not generate the allowed four generation picture even after the inclusion of a sterile neutrino.

The plan of the paper is as follows. In section 2 we discuss the atmospheric neutrino code employed for the analysis of the SK data. In section 3 we present the formalism for three-generation oscillation analysis and calculate the required probabilities. In section 4 we present the χ^2 analysis of only SK atmospheric neutrino data. In section 5 we present the combined χ^2 analysis of SK and CHOOZ data. In section 6 we compare the allowed values of mixing angles from the above analyses with those allowed by the other accelerator and reactor data including LSND. In section 7 we discuss the implications of our results for the future long baseline experiments and end in section 8 with some discussions and conclusions.

2 The Atmospheric Neutrino Code

Our atmospheric neutrino code is described in detail in [22]. This code reproduces the standard results for the two flavour $\nu_\mu - \nu_\tau$ oscillations well. In this paper we extend this code appropriately for the three-generation case. For three-generations it is convenient to define the quantities $N_{\mu_{osc}}$ and $N_{e_{osc}}$ as

$$\begin{aligned} N_{\mu_{osc}} &= N_{\mu\mu} + N_{e\mu} \\ N_{e_{osc}} &= N_{ee} + N_{\mu e} \end{aligned}$$

where the quantities $N_{e,\mu_{osc}}$ are the numbers of e -like and μ -like events in the detector and $N_{l'}$ is defined as

$$N_{l'} = n_T \int_0^\infty dE \int_{(E_{l'})_{min}}^{(E_{l'})_{max}} dE_{l'} \int_{-1}^{+1} d\cos\psi \int_{-1}^{+1} d\cos\xi \frac{1}{2\pi} \int_0^{2\pi} d\phi \\ \times \frac{d^2 F_l(E, \xi)}{dE d\cos\xi} \cdot \frac{d^2 \sigma_{l'}(E, E_{l'}, \cos\psi)}{dE_{l'} d\cos\psi} \epsilon(E_{l'}) \cdot P_{\nu_l \nu_{l'}}(E, \xi). \quad (1)$$

n_T denotes the number of target nucleons, E is the neutrino energy, $E_{l'}$ is the energy of the final charged lepton, ψ is the angle between the incoming neutrino ν_l and the scattered lepton l' , ξ is the zenith angle of the neutrino and ϕ is the azimuthal angle corresponding to the incident neutrino direction. The zenith angle of the charged lepton is given by

$$\cos\Theta = \cos\xi \cos\psi + \sin\xi \cos\phi \sin\psi \quad (2)$$

$d^2 \sigma_{l'}/dE_{l'} d\cos\psi$ is the differential cross section for $\nu_{l'} N \rightarrow l' X$ scattering, $\epsilon(E_{l'})$ is the detection efficiency for the 1 ring events in the detector and $P_{\nu_l \nu_{l'}}$ is the probability of a neutrino flavour l to convert to a neutrino of flavour l' . We use the atmospheric neutrino fluxes $\frac{d^2 F_l(E, \xi)}{dE d\cos\xi}$ from [23]. For further details of the code we refer to [22].

As a measure of the total atmospheric neutrino flux we use the double ratio R , where

$$R \equiv \frac{(N_\mu/N_e)|_{osc}}{(N_\mu/N_e)|_{no-osc}}. \quad (3)$$

To probe the up-down flux asymmetries we use the parameter Y defined in [3],

$$Y_l \equiv \frac{(N_l^{-0.2}/N_l^{+0.2})|_{osc}}{(N_l^{-0.2}/N_l^{+0.2})|_{no-osc}}. \quad (4)$$

Here $N_l^{-0.2}$ denotes the number of l -type events produced in the detector with zenith angle $\cos\Theta < -0.2$, *i.e.* the upward neutrino events while $N_l^{+0.2}$ denotes the number of l -type events for $\cos\Theta > 0.2$ *i.e.* events coming from downward neutrinos. The central bin has contributions from both upward and downward neutrinos and is not useful for studying the up-down asymmetry.

3 Three-Flavor Analysis

The general expression for the probability that an initial ν_α of energy E gets converted to a ν_β after traveling a distance L in vacuum is given by,

$$P(\nu_\alpha, 0; \nu_\beta, t) = \delta_{\alpha\beta} - 4 \sum_{j>i} U_{\alpha i} U_{\beta i} U_{\alpha j} U_{\beta j} \sin^2 \left(\frac{\pi L}{\lambda_{ij}} \right) \quad (5)$$

where λ_{ij} is defined to be the neutrino vacuum oscillation wavelength given by,

$$\lambda_{ij} = (2.47\text{m}) \left(\frac{E}{\text{MeV}} \right) \left(\frac{\text{eV}^2}{\Delta_{ij}} \right) \quad (6)$$

which denotes the scale over which neutrino oscillation effects can be significant;

$\Delta_{ij} = |m_j^2 - m_i^2|$. The actual forms of the various survival and transition probabilities depend on the spectrum of Δm^2 assumed and the choice of the mixing matrix U relating the flavor eigenstates to the mass eigenstates. We choose the flavor states $\alpha = 1, 2$, and 3 to correspond to e, μ and τ respectively. The most suitable parameterization of U for the mass spectrum chosen by us is $U = R_{13} R_{12} R_{23}$ where R_{ij} denotes the rotation matrix in the ij -plane. This yields:

$$U = \begin{pmatrix} c_{12}c_{13} & s_{12}c_{13}c_{23} - s_{13}s_{23} & c_{13}s_{12}s_{23} + s_{13}c_{23} \\ -s_{12} & c_{12}c_{23} & c_{12}s_{23} \\ -s_{13}c_{12} & -s_{13}s_{12}c_{23} - c_{13}s_{23} & -s_{12}s_{13}s_{23} + c_{13}c_{23} \end{pmatrix} \quad (7)$$

where $c_{ij} = \cos \theta_{ij}$ and $s_{ij} = \sin \theta_{ij}$ here and everywhere else in the paper. We have assumed CP-invariance so that U is real. The above choice of U has the advantage that θ_{23} does not appear in the expressions for the probabilities for the laboratory experiments [11].

The probabilities relevant for atmospheric neutrinos are

$$P_{\nu_e \nu_e} = 1 - 2c_{13}^2 c_{12}^2 + 2c_{13}^4 c_{12}^4 - 4(c_{13}s_{12}c_{23} - s_{13}s_{23})^2 (c_{13}s_{12}s_{23} + s_{13}c_{23})^2 S_{23} \quad (8a)$$

$$P_{\nu_\mu \nu_e} = 2c_{13}^2 c_{12}^2 s_{12}^2 - 4c_{12}^2 c_{23} s_{23} (c_{13}s_{12}c_{23} - s_{13}s_{23})(c_{13}s_{12}s_{23} + s_{13}c_{23}) S_{23} \quad (8b)$$

$$P_{\nu_\mu \nu_\mu} = 1 - 2c_{12}^2 s_{12}^2 - 4c_{12}^4 c_{23}^2 s_{23}^2 S_{23} \quad (8c)$$

where $S_{23} = \sin^2(\pi L/\lambda_{23})$. Apart from the most general three generation regime, the following limits are of interest, as we will see later in the context of the SK data:

1. The two-generation limits

Because of the presence of more parameters as compared to the one mass scale dominance picture there are twelve possible two-generation limits [21] with the oscillations driven by either Δ_{LSND} or Δ_{ATM} . Below we list these limits specifying the mass scales that drive the oscillations:

- $s_{12} \rightarrow 0, s_{13} \rightarrow 0$ $(\nu_\mu - \nu_\tau, \Delta_{ATM})$
 $s_{12} \rightarrow 1, s_{13} \rightarrow 0$ $(\nu_e - \nu_\tau, \Delta_{ATM})$
 $s_{12} \rightarrow 0, s_{13} \rightarrow 1$ $(\nu_\mu - \nu_e, \Delta_{ATM})$
 $s_{12} \rightarrow 1, s_{13} \rightarrow 1$ $(\nu_e - \nu_\tau, \Delta_{ATM})$
- $s_{13} \rightarrow 0, s_{23} \rightarrow 0$ $(\nu_\mu - \nu_e, \Delta_{LSND})$
 $s_{13} \rightarrow 0, s_{23} \rightarrow 1$ $(\nu_\mu - \nu_e, \Delta_{LSND})$
 $s_{13} \rightarrow 1, s_{23} \rightarrow 0$ $(\nu_\mu - \nu_\tau, \Delta_{LSND})$
 $s_{13} \rightarrow 1, s_{23} \rightarrow 1$ $(\nu_\mu - \nu_\tau, \Delta_{LSND})$
- $s_{12} \rightarrow 0, s_{23} \rightarrow 0$ $(\nu_e - \nu_\tau, \Delta_{LSND})$
 $s_{12} \rightarrow 0, s_{23} \rightarrow 1$ $(\nu_e - \nu_\tau, \Delta_{LSND})$
 $s_{12} \rightarrow 1, s_{23} \rightarrow 0$ $(\nu_e - \nu_\tau, \Delta_{ATM})$
 $s_{12} \rightarrow 1, s_{23} \rightarrow 1$ $(\nu_e - \nu_\tau, \Delta_{ATM})$

2. $s_{12}^2 = 0.0$

In this limit the relevant probabilities become

$$P_{\nu_e \nu_e} = 1 - 2c_{13}^2 s_{13}^2 + 4s_{13}^2 c_{23}^2 s_{23}^2 S_{23} \quad (9a)$$

$$P_{\nu_e \nu_\mu} = 4s_{13}^2 s_{23}^2 c_{23}^2 S_{23} \quad (9b)$$

$$P_{\nu_\mu \nu_\mu} = 1 - 4c_{23}^2 s_{23}^2 S_{23} \quad (9c)$$

Thus $P_{\nu_\mu \nu_\mu}$ is the same as the two generation limit, $P_{\nu_\mu \nu_e}$ is governed by two of the mixing angles and one mass scale and $P_{\nu_e \nu_e}$ is governed by two mixing angles and both mass scales.

3. $s_{13}^2 = 0.0$

For this case the probabilities take the form

$$P_{\nu_e \nu_e} = 1 - 2c_{12}^2 s_{12}^2 - 4s_{12}^4 c_{23}^2 s_{23}^2 S_{23} \quad (10a)$$

$$P_{\nu_e \nu_\mu} = 2c_{12}^2 s_{12}^2 - 4c_{12}^2 s_{12}^2 c_{23}^2 s_{23}^2 S_{23} \quad (10b)$$

$$P_{\nu_\mu \nu_\mu} = 1 - 2c_{12}^2 s_{12}^2 - 4c_{12}^4 c_{23}^2 s_{23}^2 S_{23} \quad (10c)$$

In this case the probabilities are governed by two mass scales and two mixing angles.

We note that for cases (2) and (3) the probabilities are symmetric under the transformation $\theta_{23} \rightarrow \pi/2 - \theta_{23}$. The probabilities for these cases are functions of at most two mixing angles as in the OMSD case [4] but they are governed by both mass scales making these limits different from the OMSD limit.

For the neutrino mass scenario considered in this paper the matter effects are not significant in general. Assuming a typical density of 5 gm/cc and $E = 10$ GeV, the matter potential $A = 2\sqrt{2}G_F n_e E \simeq 3.65 \times 10^{-3} \text{ eV}^2$. Since $\Delta_{12} = \Delta_{13} \gg A$, the matter effects can be neglected.

4 χ^2 -analysis of the SK data

We minimize the χ^2 function defined as [3]

$$\chi^2 = \sum_i \left[\left(\frac{R^{exp} - R^{th}}{\delta R^{exp}} \right)^2 + \left(\frac{Y_\mu^{exp} - Y_\mu^{th}}{\delta Y_\mu^{exp}} \right)^2 + \left(\frac{Y_e^{exp} - Y_e^{th}}{\delta Y_e^{exp}} \right)^2 \right], \quad (11)$$

where the sum is over the sub-GeV and multi-GeV cases. The experimentally observed rates are denoted by the superscript "exp" and the theoretical predictions for the quantities are labeled by "th". ΔR^{exp} is the error in R obtained by combining the statistical and systematic errors in quadrature. ΔY^{exp} corresponds to the error in Y . For this we take only the statistical errors since these are much larger compared to the systematic errors. We include both the e -like and the μ -like up-down asymmetries in the fit. Thus we have six experimental data points. The probabilities for the

atmospheric neutrinos are explicit functions of one mass-squared difference and three mixing angles making the number of degrees of freedom (d.o.f) two. The other mass squared difference gives rise to Δm^2 independent average oscillations and hence does not enter the fit as an independent parameter.

The data used are shown in Table 1 which corresponds to the 848 days of data [24].

Table 1: The 848 days of SK data used in this analysis.

Quantity	Sub – GeV	Multi – GeV
R^{exp}	0.69	0.68
ΔR^{exp}	0.054	0.089
Y_μ^{exp}	0.74	0.53
ΔY_μ^{exp}	0.04	0.047
Y_e^{exp}	1.034	0.95
ΔY_e^{exp}	0.058	0.112

For two-flavour $\nu_\mu - \nu_\tau$ oscillation the 848 days of data gives the following best-fits and χ_{min}^2 :

- $\chi_{min}^2/d.o.f. = 1.206/4$, $\Delta m^2 = 0.0028 \text{ eV}^2$, $\sin^2 2\theta = 1.0$

This corresponds to a goodness of fit of 87.7%. Our results for the best-fit values agree with that obtained by the SK group for the 848 days of data although the $\chi^2/d.o.f$ is different as the fitting procedure is different ¹.

For the general three-generation scheme the χ_{min}^2 and the best-fit values of parameters that we get are

- $\chi_{min}^2/d.o.f. = 0.995/2$, $\Delta_{23} = 0.002 \text{ eV}^2$, $s_{23}^2 = 0.5$, $s_{12}^2 = 0.02$ and $s_{13}^2 = 0.005$

¹The best-fit values for two-generation $\nu_\mu - \nu_\tau$ oscillation solution for the 848 days data, as obtained by the SK group are $\sin^2 2\theta = 0.995$, $\Delta m^2 = 3.05 \times 10^{-3} \text{ eV}^2$ with $\chi_{min}^2/d.o.f. = 55.4/67$. This corresponds to the goodness of fit of 84.3% [24].

This solution is allowed at 60.8% C.L.

Since the error distributions of R and Y have a non-Gaussian nature, question might arise as regards the use of these in performing χ^2 -analysis [25]. Detailed χ^2 -analysis using the absolute number of e or μ type events including the errors and their correlations has been done in [2, 4]. However for a high statistics experiment like SK, χ^2 analysis using these ratios is justified within the 3σ region around the best-fit point[3].

4.1 Zenith-Angle distribution

Since the probabilities in our case are in general governed by two mass scales and all three mixing angles it is difficult to understand the allowed regions. To facilitate the qualitative understanding we present in fig. 2 the histograms *viz* describe the zenith angle distribution. The event distributions in these histograms are approximately given by,

$$\frac{N_\mu}{N_{\mu 0}} \approx P_{\nu_\mu \nu_\mu} + \frac{N_{e0}}{N_{\mu 0}} P_{\nu_e \nu_\mu} \quad (12)$$

$$\frac{N_e}{N_{e0}} \approx P_{\nu_e \nu_e} + \frac{N_{\mu 0}}{N_{e0}} P_{\nu_\mu \nu_e} \quad (13)$$

where the quantities with suffix 0 indicates the no-oscillation values. For the sub-GeV data $N_{\mu 0}/N_{e0} \approx 2$ to a good approximation however for the multi-GeV data this varies in the range 2 (for $\cos \Theta = 0$) to 3 (for $\cos \Theta = \pm 1$) [4].

The dotted line in fig. 2 represent the histograms for the best-fit value for two-generation $\nu_\mu - \nu_\tau$ oscillations, for which $P_{\nu_e \nu_e} = 1$. The solid line gives the histograms for the three generation best-fit values. The figure shows that the three-generation case reproduces the electron excess slightly better than the two-generation case without altering the μ -events significantly. However since the errorbars associated with the electron events are larger, the three generation fit is not better than the one we get with two generations.

In fig. 2b we study the effect of varying s_{12}^2 and s_{13}^2 for typical values of $\Delta_{23} = 0.002 \text{ eV}^2$ and $s_{23}^2 = 0.5$ or 0.4 . The thick solid line shows the event distribution for $s_{12}^2 = 0$ and $s_{13}^2 = 0.1$. As s_{13}^2 increases from 0, keeping s_{12}^2 as 0, from eqs. (9) $P_{\nu_e \nu_e}$

decreases from 1 and $P_{\nu_e \nu_\mu}$ increases from zero resulting in a net electron depletion according to (13). The long dashed line corresponds to $s_{13}^2 = 0.3$ for which the electron depletion is too high as compared to data. The muon events are not affected much as $P_{\nu_\mu \nu_\mu}$ is independent of s_{13}^2 . There is only a slight increase governed by eq. (12) as $P_{\nu_\mu \nu_e}$ increases with increasing s_{13}^2 .

On the other hand for $s_{13}^2 = 0.0$, the effect of increasing s_{12}^2 is to increase the number of electron events and decrease the number of muon events according to eqs. (10), (13) and (12). This is shown by the short dashed and dotted lines in fig. 2b. For $s_{12}^2 = 0.2$ the electron excess and muon depletion both becomes too high as compared to the data.

For the case when both s_{12}^2 and s_{13}^2 are 0.1 the electron depletion caused by increasing s_{12}^2 and the excess caused by increasing s_{13}^2 gets balanced and the event distributions are reproduced quite well, shown by the dashed-dotted line. The thin solid line shows the effect of increasing s_{12}^2 to 0.2 keeping s_{13}^2 as 0.1. For this case although the electron excess is less compared to the case where $s_{12}^2 = 0.2$ and $s_{13}^2 = 0$, the muon depletion is more.

In fig. 2c we study the effect of varying s_{23}^2 and Δ_{23} in the limit of $s_{12}^2 = 0$ with s_{13}^2 fixed at 0.1. As discussed in section 3 if one of the mixing angles is zero there is a symmetry about $s_{23}^2 = 0.5$. Thus we present only two values of $s_{23}^2 = 0.2$ and 0.4. For fixed Δ_{23} as s_{23}^2 increases, $P_{\nu_\mu \nu_\mu}$ decreases, making the muon depletion higher. This is reflected by the thick and thin lines, for two representative values of Δ_{23} . The electron events are not affected much by change of s_{23}^2 . The slight increase with s_{23}^2 is due to increase of both $P_{\nu_e \nu_e}$ and $P_{\nu_\mu \nu_e}$. To understand the dependence on Δ_{23} we note that for $s_{23}^2 = 0.2$, $N_{\nu_\mu}/N_{\nu_{\mu 0}} \approx 1 - 0.65S_{23}$. For 0.007 eV² the contribution of S_{23} is more resulting in a lower number of muon events. For the electron events however the behavior with Δ_{23} is opposite with $N_{\nu_e}/N_{\nu_{e 0}} = 0.82 + 0.12S_{23}$. Thus with increasing Δ_{23} the number of electron events increase. Also note that since the contribution of S_{23} comes with opposite sign the zenith-angle distribution for a fixed Δ_{23} is opposite for the muon and the electron events.

In fig. 2d we show the histograms in the limit of $s_{13}^2 = 0.0$, keeping s_{12}^2 as 0.1 and varying Δ_{23} and s_{23}^2 . As s_{23}^2 increases all the relevant probabilities decrease according to eq. (10) and therefore both $N_{\nu_\mu}/N_{\nu_{\mu 0}}$ and $N_{\nu_e}/N_{\nu_{e 0}}$ decrease giving less number of events for both. For this case the S_{23} term comes with the same sign (negative) in both $N_{\nu_\mu}/N_{\nu_{\mu 0}}$ and $N_{\nu_e}/N_{\nu_{e 0}}$ (from eq. (10), (13) and (12)). Therefore the depletion is more for higher Δ_{23} for both muon and electron events.

4.2 Allowed parameter region

The solid lines in fig. 3 present the variation of the $\Delta\chi^2 = \chi^2 - \chi_{min}^2$ with respect to one of the parameters keeping the other three unconstrained, for the SK data. The dotted line shows the 99% C.L. ($= 13.28$ for 4 parameters) limit. We find that at 99% C.L. the allowed ranges include $6 \times 10^{-4} \text{ eV}^2 \leq \Delta_{23} \leq 10^{-2} \text{ eV}^2$, $0.26 \leq s_{23}^2 \leq 0.74$, $s_{12}^2 \leq 0.21$ and $s_{13}^2 \leq 0.38$.

In figs. 4a-d the solid lines give the 99% C.L. ($\chi^2 \leq \chi_{min}^2 + 13.28$ for 4 parameters) contours allowed by the SK data, projecting them into two parameter subspaces keeping the other two parameters fixed. These contours are with respect to the global χ_{min}^2 .

In fig. 4a the solid lines give the 99% C.L. allowed area from SK data in the Δ_{23} - s_{23}^2 plane keeping the values of s_{13}^2 and s_{12}^2 fixed in the allowed range of fig. 3. The first panel represents the two-generation $\nu_\mu - \nu_\tau$ oscillation limit modulo the difference in the definition of the C.L. limit as the number of parameters are different. We have seen from the histograms in fig. 2b that raising s_{12}^2 results in electron excess and muon depletion. On the other hand increase in s_{13}^2 causes electron depletion keeping the muon events nearly unaltered. The above features are reflected in the shrinking and disappearance of the allowed regions in the first row and column. In the panels where both s_{12}^2 and s_{13}^2 are nonzero one may get allowed regions only when the electron depletion due to increasing s_{13}^2 is replenished by the increase in s_{12}^2 .

In fig. 4b we present the 99% C.L. allowed areas in the bilogarithmic $\tan^2 \theta_{12} - \tan^2 \theta_{13}$ plane for various values of the parameters Δ_{23} and s_{23}^2 , the range of which is chosen from fig. 3. We use the $\log(\tan)$ representation which enlarges the allowed

regions at the corners and the clarity is enhanced. The four corners in this plot refer to the two-generation limits discussed in section 3. The extreme left corner ($\theta_{12} \rightarrow 0, \theta_{13} \rightarrow 0$) correspond to the two generation $\nu_\mu - \nu_\tau$ oscillation limit. As we move up increasing θ_{13} one has in addition $\nu_e - \nu_\mu$ and $\nu_e - \nu_\tau$ mixing and the χ^2 increases. Around $\theta_{13} = \pi/4$ these effects are maximum and one gets a very high χ^2 . As $\theta_{13} \rightarrow 1$ one goes to the two generation $\nu_\mu - \nu_e$ oscillation region and the χ^2 again decreases but it is still quite high to be allowed. For the best-fit values of Δ_{23} and θ_{23} if we take θ_{12} and θ_{13} to be 0 and $\pi/2$ respectively then the χ^2_{min} is 59.57 which is therefore ruled out. Both the right hand corners in these plots refer to pure $\nu_e - \nu_\tau$ oscillations and therefore there are no allowed regions in these zones.

In fig. 4c the solid lines show the 99% C.L. allowed regions from SK data in the $s_{23}^2 - s_{12}^2$ plane for fixed values of Δ_{23} and s_{13}^2 . In contrast to the previous figure, here (and in the next figure) we use the sin – sin representation because the allowed regions are around $\theta_{23} = \pi/4$ and this region gets compressed in the $\log(\tan) - \log(\tan)$ representation. For explaining the various allowed regions we separate the figures in two sets

- For $s_{13}^2 = 0.0$, the four corners of the panels represent the no-oscillation limits inconsistent with the data. Also as discussed in section 3 for $s_{23}^2 = 0.0$ or 1.0 one goes to the limit of pure $\nu_\mu - \nu_e$ conversions driven by Δ_{LSND} , which is not consistent with data. One obtains allowed regions only when s_{23}^2 is close to 0.5 with s_{12}^2 small, so that one goes to the two generation $\nu_\mu - \nu_\tau$ conversion limit. The allowed range of s_{12}^2 is controlled mainly by the electron excess as has been discussed before while the allowed range of s_{23}^2 is determined mostly by the muon depletion.
- For $s_{13}^2 \neq 0$, the four corners represent the two-generation $\nu_e - \nu_\tau$ oscillation limit discussed in section 3 and hence these corners are not allowed. For $s_{23}^2 = 0.0$ or 1.0 and $s_{12}^2 \neq 0$ or 1 one has Δ_{LSND} driven $\nu_\mu - \nu_e$ and $\nu_\mu - \nu_\tau$ conversion and Δ_{ATM} driven $\nu_e - \nu_\tau$ conversions. This scenario is not allowed as it gives excess of electron events and also fails to reproduce the correct zenith angle dependence.

For a fixed Δ_{23} as s_{13}^2 increases the electron depletion increases and the allowed region decreases in size. The effect of increasing s_{13}^2 can be balanced by increasing s_{12}^2 which increases the number of electron events and hence for a fixed Δ_{23} the allowed regions shift towards higher s_{12}^2 values.

In fig. 4d the solid contours refer to the 99% C.L. allowed areas from SK atmospheric neutrino data in the $s_{13}^2 - s_{23}^2$ plane for various values of Δ_{23} and s_{12}^2 .

- For $s_{12}^2 = 0.0$ the corners represent no oscillation limits. In the limit $s_{23}^2 \rightarrow 0$ or 1, one gets $\nu_e - \nu_\tau$ oscillation driven by Δ_{LSND} which is also not allowed. For $s_{13}^2 = 0.0$ and $s_{23}^2 \sim 0.5$ one has maximal two-flavour $\nu_\mu - \nu_\tau$ oscillation limit which is therefore allowed. As seen from the histograms in fig. 2b as s_{13}^2 increases the electron depletion becomes higher and that restricts higher s_{13}^2 values.
- For $s_{12}^2 \neq 0$, the four corners represent two-generation limits driven by Δ_{LSND} . This is the regime of average oscillations and cannot explain the zenith angle dependence of the data. For a fixed Δ_{23} the allowed region first expands and then shrinks in size and also shifts towards higher s_{13}^2 values as s_{12}^2 increases.

5 χ^2 analysis of the SK + CHOOZ data

The CHOOZ experiment can probe upto 10^{-3} eV² and hence it can be important to cross-check the atmospheric neutrino results. In particular a two-generation analysis shows that CHOOZ data disfavors the $\nu_\mu - \nu_e$ solution to the atmospheric neutrino problem. The general expression for the survival probability of the electron neutrino in presence of three flavours is

$$P_{\nu_e \nu_e} = 1 - 4U_{e1}^2(1 - U_{e1}^2)\sin^2 \pi L/\lambda_{12} - 4U_{e2}^2 U_{e3}^2 \sin^2(\pi L/\lambda_{23}) \quad (14)$$

This is the most general expression without the one mass scale dominance approximation. We now minimize the χ^2 defined as

$$\chi^2 = \chi_{ATM}^2 + \chi_{CHOOZ}^2 \quad (15)$$

where we define χ^2_{CHOOZ} as [3]

$$\chi^2_{CHOOZ} = \sum_{j=1,15} \left(\frac{x_j - y_j}{\Delta x_j} \right)^2 \quad (16)$$

where x_j are the experimental values, y_j are the corresponding theoretical predictions and the sum is over 15 energy bins of data of the CHOOZ experiment [5]. We use the latest CHOOZ result. For the CHOOZ experiment the $\sin^2 \pi L/\lambda_{12}$ term does not always average out to 0.5 and one has to do the energy integration properly. For our analysis we keep the Δ_{12} fixed at 2 eV² and do a four parameter fit as in SK (for SK this term always averages to 0.5). The χ^2_{min} and the best-fit values of parameters that we get are

- $\chi^2_{min}/d.o.f. = 7.54/17$, $\Delta_{23} = 0.0028$ eV², $s_{23}^2 = 0.5$, $s_{12}^2 = 4 \times 10^{-4}$ and $s_{13}^2 = 0.0$.

Thus the best-fit values shift towards the two-generation limit when we include the CHOOZ result. This provides a very good fit to the data being allowed at 97% C.L.

The dashed lines in fig. 3 give the combined SK+CHOOZ $\Delta\chi^2 (= \chi^2 - \chi^2_{min})$ given by eq. (15), as a function of one of the parameters, keeping the other three unconstrained. We find that the CHOOZ data severely restricts the allowed ranges for the parameters s_{12}^2 and s_{13}^2 to values $\lesssim 0.04$, while Δ_{23} and s_{23}^2 are left almost unaffected. Since CHOOZ is consistent with no oscillation one requires $P_{\nu_e \nu_e}$ close to 1. So the second and the third terms in eq. (14) should separately be very small. The second term implies U_{e1}^2 to be close to either 0 or 1. U_{e1}^2 close to zero implies either s_{12}^2 or s_{13}^2 close to 1 which is not consistent with SK. Therefore U_{e1}^2 is close to 1. Then from unitarity both U_{e2}^2 and U_{e3}^2 are close to 0 and so the third term goes to zero irrespective of the value of Δ_{23} and s_{23}^2 .

The 99% C.L. regions allowed by a combined analysis of SK and CHOOZ data is shown by the dotted lines in figs. 4a-d. It is seen that most of the regions allowed by the three-flavour analysis of the SK data is ruled out when we include the CHOOZ result. The CHOOZ constraint affects the two mixing angles s_{12}^2 and s_{13}^2 more. The range of Δ_{23} and s_{23}^2 remain more or less stable to SK values. None of the allowed

regions shown in fig. 4a are allowed excepting the two-generation $\nu_\mu - \nu_\tau$ oscillation limit because CHOOZ does not allow such high values of either s_{13}^2 or s_{12}^2 . In fig. 5 we present the allowed regions in the $\Delta_{23} - s_{23}^2$ plane for various fixed values of s_{12}^2 and s_{13}^2 , determined from the dashed lines in fig. 3. The solid lines in fig. 5 give the 99% C.L. area allowed by the SK data while the dotted lines give the corresponding allowed region from the combined analysis of SK+CHOOZ. We find that for the combined analysis we get allowed regions in this plane only for much smaller values of s_{12}^2 and s_{13}^2 , which ensures that the electron events are neither less nor more than expectations.

6 Combined allowed area from short baseline accelerator and reactor experiments

As mentioned earlier the higher mass scale of this scenario can be explored in the accelerator based neutrino oscillation search experiments. For the mass-pattern considered the most constraining accelerator experiments are LSND [7], CDHSW [26], E531 [27] and E776 [28]. Among these only LSND reported positive evidence of oscillation. Other experiments are consistent with no-oscillation hypothesis. Also important in this mass range are the constraints from the reactor experiment Bugey [29]. The relevant probabilities are [11]

- Bugey

$$P_{\bar{\nu}_e \bar{\nu}_e} = 1 - 4c_{13}^2 c_{12}^2 \sin^2(\pi L/\lambda_{12}) + 4c_{13}^4 c_{12}^4 \sin^2(\pi L/\lambda_{12}) \quad (17)$$

- CDHSW

$$P_{\bar{\nu}_\mu \bar{\nu}_\mu} = 1 - 4c_{12}^2 s_{12}^2 \sin^2(\pi L/\lambda_{12}) \quad (18)$$

- LSND and E776

$$P_{\bar{\nu}_\mu \bar{\nu}_e} = 4c_{12}^2 s_{12}^2 c_{13}^2 \sin^2(\pi L/\lambda_{12}) \quad (19)$$

- E531

$$P_{\nu_\mu \nu_\tau} = 4c_{12}^2 s_{12}^2 s_{13}^2 \sin^2(\pi L/\lambda_{13}) \quad (20)$$

We note that the probabilities are functions of one of the mass scales and two mixing angles. Thus the one mass scale dominance approximation applies. There are many analyses in the literature of the accelerator and reactor data including LSND under this one mass scale dominance assumption [11, 30]. These analyses showed that when one considers the results from the previous accelerator and reactor experiments there are three allowed regions in the $\theta_{12} - \theta_{13}$ plane

- low θ_{12} - low θ_{13}
- low θ_{12} - high θ_{13}
- high θ_{12} - θ_{13} unconstrained

When the LSND result is combined with these results then only the first and the third zones remain allowed in the mass range $0.5 \leq \Delta_{12} \leq 2 \text{ eV}^2$. This is shown in fig. 6 for two representative values of $\Delta_{12} - 0.5 \text{ eV}^2$ and 2 eV^2 . For higher mass values there are no combined allowed region. The light-shaded area in fig. 6 shows the 90% C.L. allowed area in the bilogarithmic $\tan^2 \theta_{12} - \tan^2 \theta_{13}$ plane from the observance of no-oscillation in the above mentioned accelerator and reactor experiments. The 90% allowed region by the LSND experiment is within the dashed lines. The solid line shows the 90% C.L. ($\chi^2 \leq \chi_{min}^2 + 7.78$) region allowed by the combined χ^2 analysis of the SK+CHOOZ data keeping Δ_{23} and s_{23}^2 at 0.002 eV^2 and 0.5 respectively. The combined SK atmospheric and the CHOOZ reactor data rule out the third zone (high θ_{12} with θ_{13} unconstrained) allowed from LSND and other accelerator and reactor experiments. Thus if one takes into account constraints from all experiments only a small region in the first zone (small θ_{12}, θ_{13}) remains allowed. This common allowed region is shown as a dark-shaded area in the fig. 6. The combined area in fig. 6, drawn for the above mentioned values of Δ_{23} and s_{23}^2 shows that in the first zone (small θ_{12}, θ_{13}), SK+CHOOZ data is less restrictive than the LSND and other accelerator reactor data. However for other combinations of Δ_{23} and s_{23}^2 one may find that the SK+CHOOZ analysis may become more restrictive at 90% C.L., atleast for θ_{13} .

7 Implications

From our analysis of the SK atmospheric data the explicit form for the 3×3 mixing matrix U at the best-fit values of parameters is

$$U = \begin{pmatrix} 0.987 & 0.050 & -0.150 \\ -0.141 & 0.700 & 0.700 \\ -0.07 & -0.712 & 0.698 \end{pmatrix} \quad (21)$$

From the combined SK+CHOOZ analysis the mixing matrix at the best-fit values of the parameters is

$$U = \begin{pmatrix} 0.997 & 0.017 & 0.017 \\ -0.024 & 0.707 & 0.707 \\ -0.07 & -0.707 & 0.707 \end{pmatrix} \quad (22)$$

From the combined allowed area of fig. 6 the mixing matrix at $\Delta_{12} = 0.5 \text{ eV}^2$, $\Delta_{23} = 0.0028 \text{ eV}^2$, $s_{12}^2 = 0.005$, $s_{13}^2 = 0.001$ and $s_{23}^2 = 0.5$, is

$$U = \begin{pmatrix} 0.999 & 0.028 & 0.072 \\ -0.07 & 0.707 & 0.707 \\ -0.032 & -0.708 & 0.705 \end{pmatrix} \quad (23)$$

Thus the allowed scenario corresponds to the one where $\langle \nu_1 | \nu_e \rangle$ is close to 1 while the states ν_2 and ν_3 are combinations of nearly maximally mixed ν_μ and ν_τ ².

Long baseline (LBL) experiments can be useful to confirm if the atmospheric neutrino anomaly is indeed due to neutrino oscillations, using well monitored accelerator neutrino beams. Some of the important LBL experiments are K2K (KEK to SK, $L \approx 250 \text{ km}$) [31], MINOS (Fermilab to Soudan, $L \approx 730 \text{ km}$) [32] and the proposed CERN to Gran Sasso experiments ($L \approx 730 \text{ km}$) [33]. In this section we explore the sensitivity of the LBL experiment K2K in probing the parameter spaces allowed by the SK+CHOOZ and other accelerator and reactor experiments including LSND. K2K

² Thus this scenario is the same as the one termed 3a in Table VI in the pre-SK analysis of [13]. In their notation the states 2 and 3 were 1 and 2. It was disfavoured from solar neutrino results.

will look for ν_μ disappearance as well as ν_e appearance. In fig. 7 we show the regions in the $\Delta_{23} - s_{23}^2$ plane that can be probed by K2K using their projected sensitivity from [31]. The top left panel is for the two-generation $\nu_\mu - \nu_\tau$ limit. The other panels are for different fixed values of s_{12}^2 and s_{13}^2 while Δ_{12} is fixed at 2 eV^2 . For LBL experiments the term containing Δ_{12} averages to 0.5 as in the atmospheric case. The solid lines in the panels show the region that can be probed by K2K using the ν_μ disappearance channel while the dotted lines give the 90% C.L. contours allowed by SK+CHOOZ. One finds that for $\Delta_{23} \geq 2 \times 10^{-3} \text{ eV}^2$, the whole region allowed by SK+CHOOZ can be probed by the ν_μ disappearance channel in K2K. The dashed lines show the 90% C.L. area that K2K can probe by the ν_e appearance mode. As s_{12}^2 increases the constraint from the $P_{\nu_\mu \nu_e}$ channel becomes important as is seen in the top right panel of fig. 7. However such high values of s_{12}^2 , although allowed by SK+CHOOZ, is not favoured when one combines LSND and other accelerator and reactor results. For lower s_{12}^2 values allowed by all the accelerator, reactor and SK atmospheric neutrino experiment the projected sensitivity in the $\nu_\mu - \nu_e$ channel of K2K is not enough to probe the allowed regions in the $\Delta_{23} - s_{23}^2$ plane as is shown by the absence of the dashed curves in the lower panels.

In fig. 8 we show the regions in the bilogarithmic $\tan^2 \theta_{12} - \tan^2 \theta_{13}$ plane which can be probed by K2K. For drawing these curves we fix $\Delta_{23} = 0.002 \text{ eV}^2$, $s_{23}^2 = 0.5$ and $\Delta_{12} = 0.5 \text{ eV}^2$. The area between the solid (dashed) lines corresponds to the region that can be explored by the $\nu_\mu - \nu_\mu$ ($\nu_\mu - \nu_e$) channel in K2K at 90% C.L.. The area within the dotted line is allowed by SK+CHOOZ and the dark shaded area is allowed by the combination of all the accelerator, reactor and SK atmospheric neutrino data at 90% C.L.. It is clear from the figure that the sensitivity in K2K in both channels is not sufficient to probe the combined allowed region in the $\theta_{12} - \theta_{13}$ plane.

The projected sensitivities of MINOS and the CERN to ICARUS proposals are lower than K2K and it will be interesting to check if one can probe the regions allowed in this picture better in these experiments. However since in our case the OMSD approximation is not applicable one has to do the energy averaging properly to get

the corresponding contours in the three-generation parameters space, and one cannot merely scale the allowed regions from the two-generation plots. For K2K we could use the fig. 5 of [31] to circumvent this problem. However since the analogous information for MINOS and CERN-Gran Sasso proposals is not available to us we cannot check this explicitly.

An important question in this context is whether one can distinguish between the OMSD three generation and this mass scheme. In both pictures the SK atmospheric neutrino data can be explained by the dominant $\nu_\mu - \nu_\tau$ oscillations mixed with little amount of $\nu_e - \nu_\mu(\nu_\tau)$ transition. However the mixing matrix U is different. A distinction can be done if one can measure the mixing angles very accurately.

What is the prospect in LBL experiments to distinguish between these pictures? We give below a very preliminary and qualitative discussion on this. If we take $s_{12}^2 = 0.02$, $s_{13}^2 = 0.02$ and $s_{23}^2 = 0.5$, $P_{\nu_\mu\nu_e}$ would be $(0.038 + 0.0004 \langle S_{23} \rangle)$. As the second term is negligible one has average oscillations. This is different from the OMSD limit where $P_{\nu_\mu\nu_e} = 4U_{\mu 3}^2 U_{e 3}^2 S_{23}$ is energy dependent. If one combines the other accelerator and reactor experiments including LSND then the allowed values of s_{12}^2 and s_{13}^2 are even less and choosing $s_{12}^2 = 0.005$, $s_{13}^2 = 0.001$ and $s_{23}^2 = 0.5$ we get $P_{\nu_e\nu_\mu} = 0.01 - 0.004 \langle S_{23} \rangle$. Here also the term involving $\langle S_{23} \rangle$ is one order of magnitude smaller and the oscillations will be averaged. Thus this channel has different predictions for the OMSD limit and beyond the OMSD limit.

8 Discussions and Conclusions

In this paper we have done a detailed χ^2 analysis of the SK atmospheric neutrino data going beyond the OMSD approximation. The mass spectrum chosen is such that $\Delta_{12} = \Delta_{13} = 0.5 - 2 \text{ eV}^2$ to explain the LSND data and Δ_{23} is in the range suitable for the atmospheric neutrino problem. If one believes in the LSND result then this three generation picture is the natural choice which can be extended to give an allowed four neutrino scenario where a sterile neutrino can be added to explain the solar neutrino

result³.

We first examine in detail what are the constraints obtained from only SK data considering its overwhelming statistics. The allowed regions include

- the two-generation $\nu_\mu - \nu_\tau$ limit (both s_{12}^2 and s_{13}^2 zero)
- regions where either s_{12}^2 or s_{13}^2 is zero; in this limit the probabilities are functions in general of two mixing angles and two mass scales.
- the three-generation regions with all three mixing angles non-zero and the probabilities governed by both mass scales.

The last two cases correspond to dominant $\nu_\mu - \nu_\tau$ oscillation with small admixture of $\nu_\mu - \nu_e$ and $\nu_e - \nu_\tau$ oscillation. We present the zenith angle distributions of the events in these cases. With the inclusion of the CHOOZ result the allowed ranges of the mixing angles s_{12}^2 and s_{13}^2 is constrained more ($\lesssim 0.03$), however the allowed ranges of Δ_{23} and s_{23}^2 do not change much (see fig. 3). When one includes the constraints from LSND and other accelerator and reactor experiments the allowed ranges get restricted further to $s_{12}^2 < 0.001$ (at 90% C.L.) and $s_{13}^2 < 0.01$ (at 90% C.L.). The precise values depend on the Δ_{12} chosen as is seen from fig. 6.

In our paper we use the ratios R and Y for doing the χ^2 -analysis as in [3]. The ratios have the advantage, that they are relatively insensitive to the uncertainties in the neutrino fluxes and cross-sections as the overall normalization factor gets canceled out. The alternative is to use the absolute number of events and perform a bin-by-bin analysis [2, 4]. But the best-fit points and the allowed regions in the two approaches do not differ much. The zenith-angle distribution of the events presented in figs 2a-d is independent of the data fitting procedure used. The allowed parameter regions estimated from these figures agree well with that obtained from the χ^2 -analysis.

To conclude, one can get allowed regions from the SK atmospheric neutrino data where both the mass scales and all the three mixing angles are relevant. With the

³ An alternative four neutrino scenario is possible where the sterile neutrino can be used to explain the atmospheric neutrino problem.

inclusion of the CHOOZ, LSND and other accelerator, reactor results, these regions are constrained severely. It is, in principle, possible to get some signatures in the LBL experiments to distinguish this picture from the OMSD limit.

The authors wish to thank Kate Scholberg for providing the 848 days SK atmospheric data.

References

- [1] Y. Fukuda *et al.*, The Super-Kamiokande Collaboration, Phys. Lett. **B433**, 9 (1998); Phys. Lett. **B436**, 33 (1998); Phys. Rev. Lett. **81**, 1562 (1998).
- [2] M.C. Gonzalez-Garcia, H. Nunokawa, O.L.G. Peres, T. Stanev, J.W.F. Valle, Phys. Rev. **D58**, 033004 (1998); M.C. Gonzalez-Garcia, H. Nunokawa, O.L.G. Peres, J.W.F. Valle, Nucl. Phys. **B543**, 3 (1999); N. Fornengo, M.C. Gonzalez-Garcia, J.W.F. Valle, hep-ph/0002147.
- [3] R. Foot, R.R. Volkas and O. Yasuda, Phys. Rev. **D58** 013006, (1998) .
- [4] G.L. Fogli, E. Lisi, A. Marrone, G. Scioscia, Phys. Rev. **D59**, 033001, (1998).
- [5] M. Apollonio *et al.*, Phys. Lett. **B 420**, 397 (1998); Phys. Lett. **B 466**, 415 (1999).
- [6] O. Yasuda, Phys. Rev.**D 58**,091301, (1998); hep-ph/9809205, to be published in the proceedings of Symposium on new era in neutrino physics, Tokyo, Japan, 11-12 June, 1998.
- [7] C. Athanassopoulos *et al.*, Phys. Rev. Lett. **75**, 2650 (1995); C. Athanassopoulos *et al.*, Phys. Rev. Lett. **81**, 1774 (1998).
- [8] V. Barger, *et al.*, Phys. Lett. **B93**, 195 (1980); J. Phys. G **6**, L165 (1980); V. Barger, K. Whisnant and R.J.N. Phillips, Phys. Rev **D22**, 1636 (1980); A. De Rújula *et al.*, Nucl. Phys. **B168**, 54 (1980).

- [9] G.L. Fogli, E. Lisi and D. Montanio, Phys. Rev. **D49**, 3626 (1994).
- [10] H. Minakata, Phys. Rev. **D52**, 6630 (1995).
- [11] S. Goswami, K. Kar and A. Raychaudhuri, hep-ph/9505395, Int. J. Mod. Phys. **A12**, 781 (1997).
- [12] A. Acker and S. Pakvasa, Phys. Lett. **B397**, 209 (1997).
- [13] G.L. Fogli, E. Lisi, D. Montanino and G. Scioscia, Phys. Rev. **D56**, 4365 (1997).
- [14] R.P. Thun and S. McKee, Phys. Lett. **B439**, 123 (1998); G. Marengo and F. Scheck, *ibid* **B440**, 332 (1998); G. Conforto, M. Barone and C. Grimani, *ibid* **B447**, 122 (1999).
- [15] T. Ohlsson and H. Snellman, Phys. Rev. **D60**, 093007 (1999).
- [16] G.L. Fogli, E. Lisi, A. Marrone and G. Scioscia, hep-ph/9906450.
- [17] C. Meier, T. Ohlsson, hep-ph/9910270.
- [18] J.N. Bahcall, P.I. Krastev and A. Yu. Smirnov, Phys. Rev. **D58**, 096016 (1999).
- [19] S.M. Bilenky, C. Giunti, W. Grimus, Phys. Rev. **D57**, 1920 (1998); Phys. Rev. **D58**, 033001 (1998).
- [20] J.J. Gomez-Cadenas and M.C. Gonzalez-Garcia, Zeit. Phys. **C71**, 443 (1996); N. Okada and O. Yasuda, Int. J. Mod. Phys. **A12**, 3669 (1997).
- [21] S. Goswami, Phys. Rev. **D55**, 2931 (1997)
- [22] S. Choubey and S. Goswami, hep-ph/9904257, to be published in Astroparticle Physics.
- [23] M. Honda, T. Kajita, S. Midorikawa, and K. Kasahara, Phys. Rev. **D52**, 4985 (1995).

- [24] K.Scholberg, private communication.
- [25] G.L. Fogli and E. Lisi, Phys. Rev. **D52**, 2775 (1995).
- [26] F. Dydak *et al.*, Phys. Lett. **B314**, 281 (1984).
- [27] N. Ushida *et al.*, Phys. Rev. Lett. **57**, 2898 (1986).
- [28] L. Borodovsky *et al.*, Phys. Rev. Lett. **68**, 274 (1992).
- [29] B. Achkar *et al.*, Nucl. Phys. **B434**, 503 (1995).
- [30] G.L. Fogli, E. Lisi and G. Scioscia, Phys. Rev. **D52**, 5334 (1995).
- [31] Y. Oyama, hep-ex/9803014.
- [32] MINOS Collaboration, "Neutrino Oscillation Physics at Fermilab": The NuMI-MINOS Project," Report NuML-L-375 (1998),
http://www.hep.anl.gov/ndk/hypertext/numi_notes.html.
- [33] C. Acquistapace *et al.*, "The CERN Neutrino beam to Gran Sasso (NGS), INFN/AE-98/05 (1998).

Figure Captions

Fig. 1: The two possible neutrino mass spectra in a three generation scheme.

Fig. 2a: The dotted (solid) line gives the zenith angle distribution of the lepton events for the best-fit cases of the two-generation (three-generation) oscillation solutions for SK. N is the number of events as given by eq. (1) and N_0 is the corresponding number with survival probability 1. The panels labelled SG_α and MG_α (α can be e or μ) give the histograms for the sub-GeV and multi-GeV α -events respectively. Also shown are the SK experimental data points with $\pm 1\sigma$ error bars.

Fig. 2b: The zenith angle distribution of the lepton events with $\Delta_{23} = 0.002 \text{ eV}^2$ and $s_{23}^2 = 0.4$ or 0.5 for various combinations of s_{12}^2 and s_{13}^2 . The SK experimental data points with the $\pm 1\sigma$ errorbars are shown.

Fig. 2c: Same as in fig. 2b for fixed $s_{12}^2 = 0.1$ and $s_{13}^2 = 0.0$ varying Δ_{23} and s_{23}^2 .

Fig. 2d: Same as in fig. 2b fixing $s_{12}^2 = 0.0$ and $s_{13}^2 = 0.1$ for different Δ_{23} and s_{23}^2 values.

Fig. 3: The variation of $\Delta\chi^2 = \chi^2 - \chi_{min}^2$ with one of the parameters keeping the other three unconstrained. The solid line corresponds to only SK data while the dashed curve gives the same for SK+CHOOZ. The dotted line shows the 99% C.L. limit for 4 parameters.

Fig. 4a: The allowed parameter regions in the $\Delta_{23} - s_{23}^2$ plane for various fixed values of s_{12}^2 and s_{13}^2 , shown at the top of each panel. The solid lines corresponds to the 99% C.L. contours from the SK data alone, while the dotted line gives the 99% contour from the combined analysis of the SK+CHOOZ data.

Fig. 4b: Same as 4a but in the bilogarithmic $\tan^2 \theta_{12} - \tan^2 \theta_{13}$ plane for fixed values

of Δ_{23} and s_{23}^2 .

Fig. 4c: Same as 4a but in the $s_{12}^2 - s_{23}^2$ plane for fixed values of s_{13}^2 and Δ_{23} .

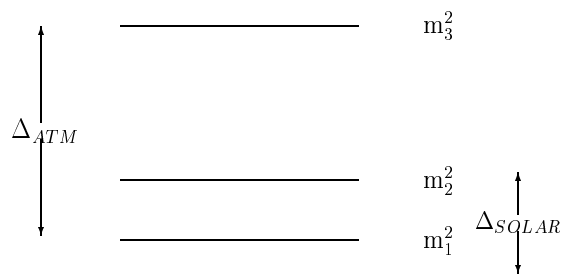
Fig. 4d: Same as 4a but in the $s_{13}^2 - s_{23}^2$ plane for various fixed values of s_{12}^2 and Δ_{23} .

Fig. 5: Same as 4a but for smaller values of s_{12}^2 and s_{13}^2 , chosen from the range determined by the SK+CHOOZ dashed line in fig. 3.

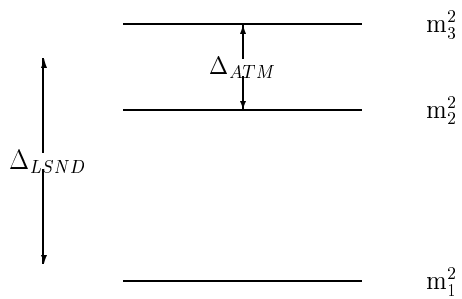
Fig. 6: The area between the dashed lines is the 90% C.L. region allowed by LSND while the light shaded zone gives the 90% C.L. allowed region from the non-observance of neutrino oscillation in the other short baseline accelerator and reactor experiments. The 90% C.L. allowed region from SK+CHOOZ analysis is within the solid line. The dark shaded area corresponds to the combined allowed region.

Fig. 7: 90% C.L. regions in the $\Delta_{23} - s_{23}^2$ plane that can be explored by the $\nu_\mu - \nu_\mu$ (solid line) and $\nu_\mu - \nu_e$ (dashed line) oscillation channels in the K2K experiment. The area inside the dotted line shows the 90% C.L. region allowed by SK+CHOOZ. The curves are presented for fixed values of s_{12}^2 and s_{13}^2 with $\Delta_{12} = 2 \text{ eV}^2$.

Fig. 8: Sensitivity of the K2K experiment in the $\tan^2 \theta_{12} - \tan^2 \theta_{13}$ plane for $\Delta_{23} = 0.002 \text{ eV}^2$, $s_{23}^2 = 0.5$ and $\Delta_{12} = 0.5 \text{ eV}^2$. The region between the solid (dashed) line gives the area that K2K can explore in the $\nu_\mu - \nu_\mu$ ($\nu_\mu - \nu_e$) channel. The 90% C.L. region allowed by SK+CHOOZ is within the dotted line. The shaded area represents the combined allowed zone from all accelerator/reactor experiments and SK+CHOOZ analysis.



(a)



(b)

Fig. 1

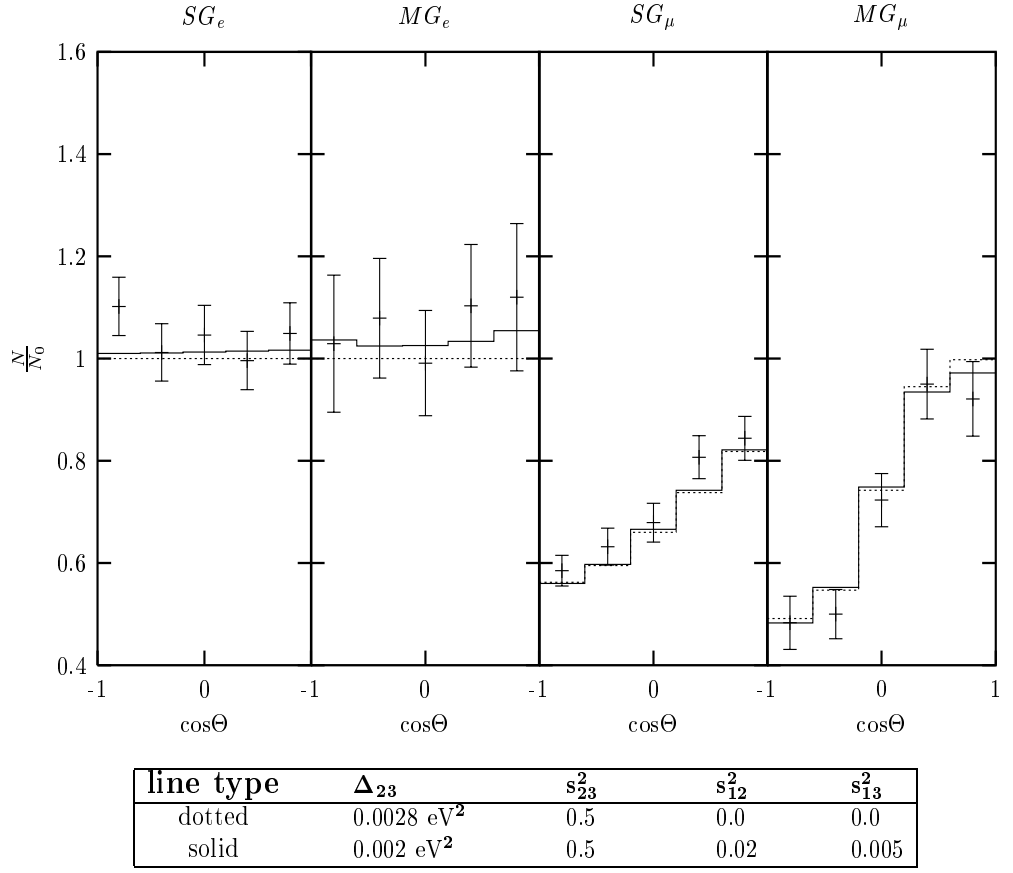
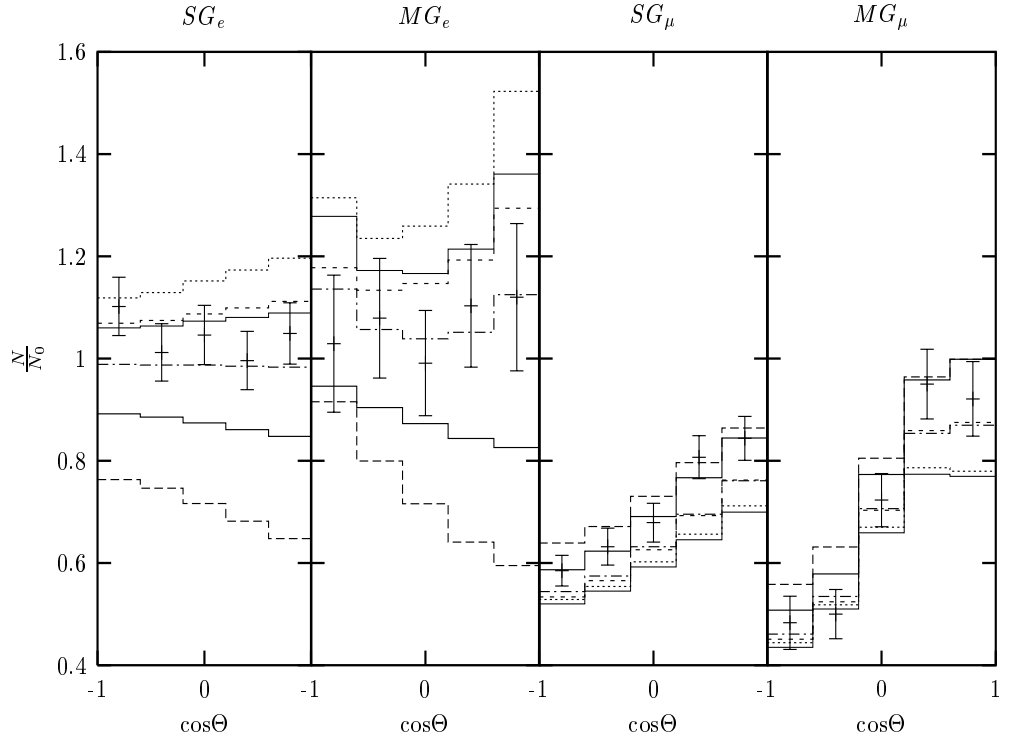
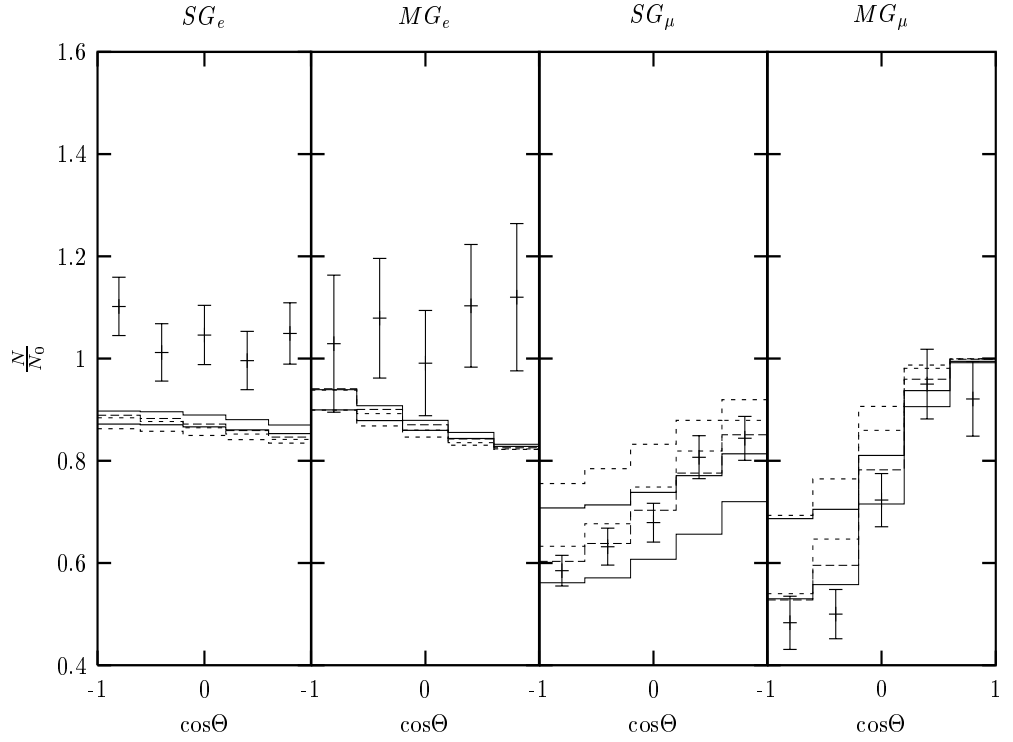


Fig. 2a



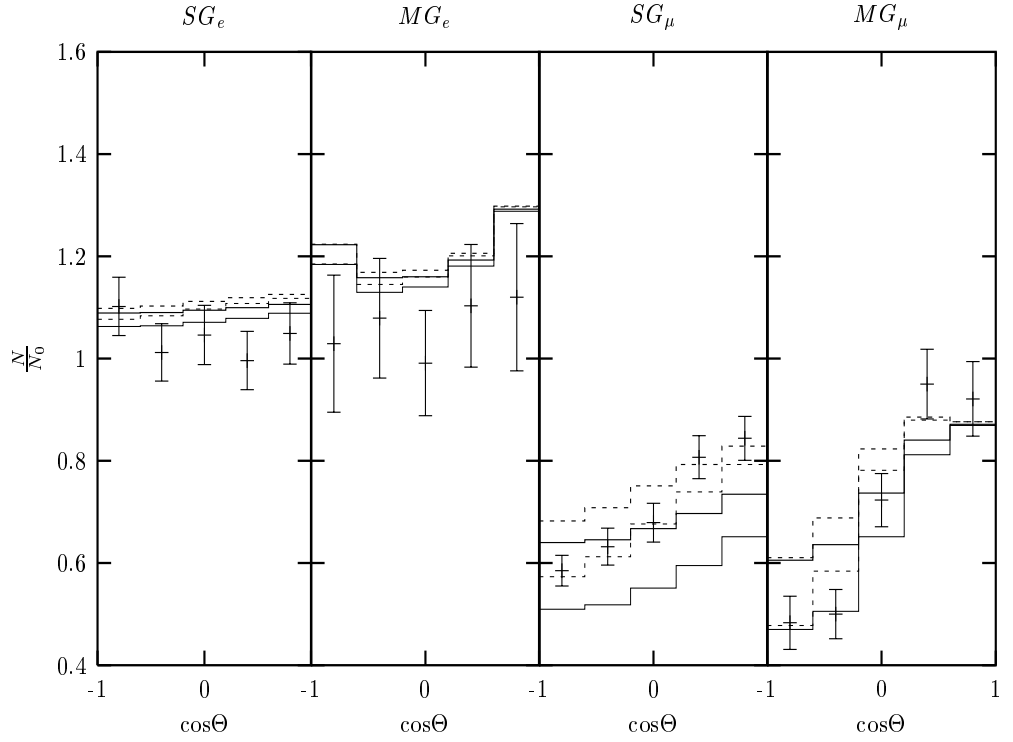
line type	Δ_{23}	s_{23}^2	s_{12}^2	s_{13}^2
thick solid	0.002 eV^2	0.5	0.0	0.1
long dashed	0.002 eV^2	0.4	0.0	0.3
short dashed	0.002 eV^2	0.5	0.1	0.0
dotted	0.002 eV^2	0.4	0.2	0.0
dashed-dotted	0.002 eV^2	0.5	0.1	0.1
thin solid	0.002 eV^2	0.5	0.2	0.1

Fig. 2b



line type	Δ_{23}	s_{23}^2	s_{12}^2	s_{13}^2
thick solid	0.007 eV^2	0.2	0.0	0.1
thick short dashed	0.0007 eV^2	0.2	0.0	0.1
thin solid	0.007 eV^2	0.4	0.0	0.1
thin short dashed	0.0007 eV^2	0.4	0.0	0.1

Fig. 2c



line type	Δ_{23}	s_{23}^2	s_{12}^2	s_{13}^2
thick solid	0.007 eV^2	0.2	0.1	0.0
thick short dashed	0.0007 eV^2	0.2	0.1	0.0
thin solid	0.007 eV^2	0.4	0.1	0.0
thin short dashed	0.0007 eV^2	0.4	0.1	0.0

Fig. 2d

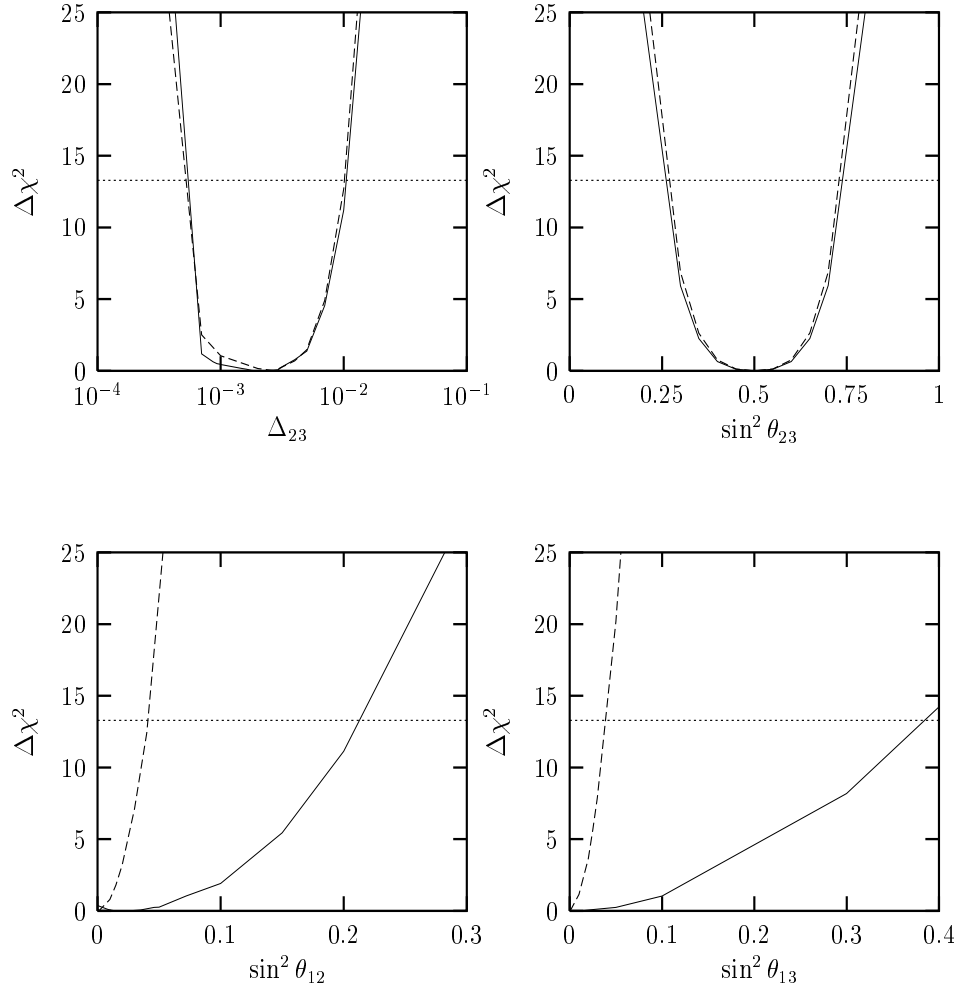


Fig. 3

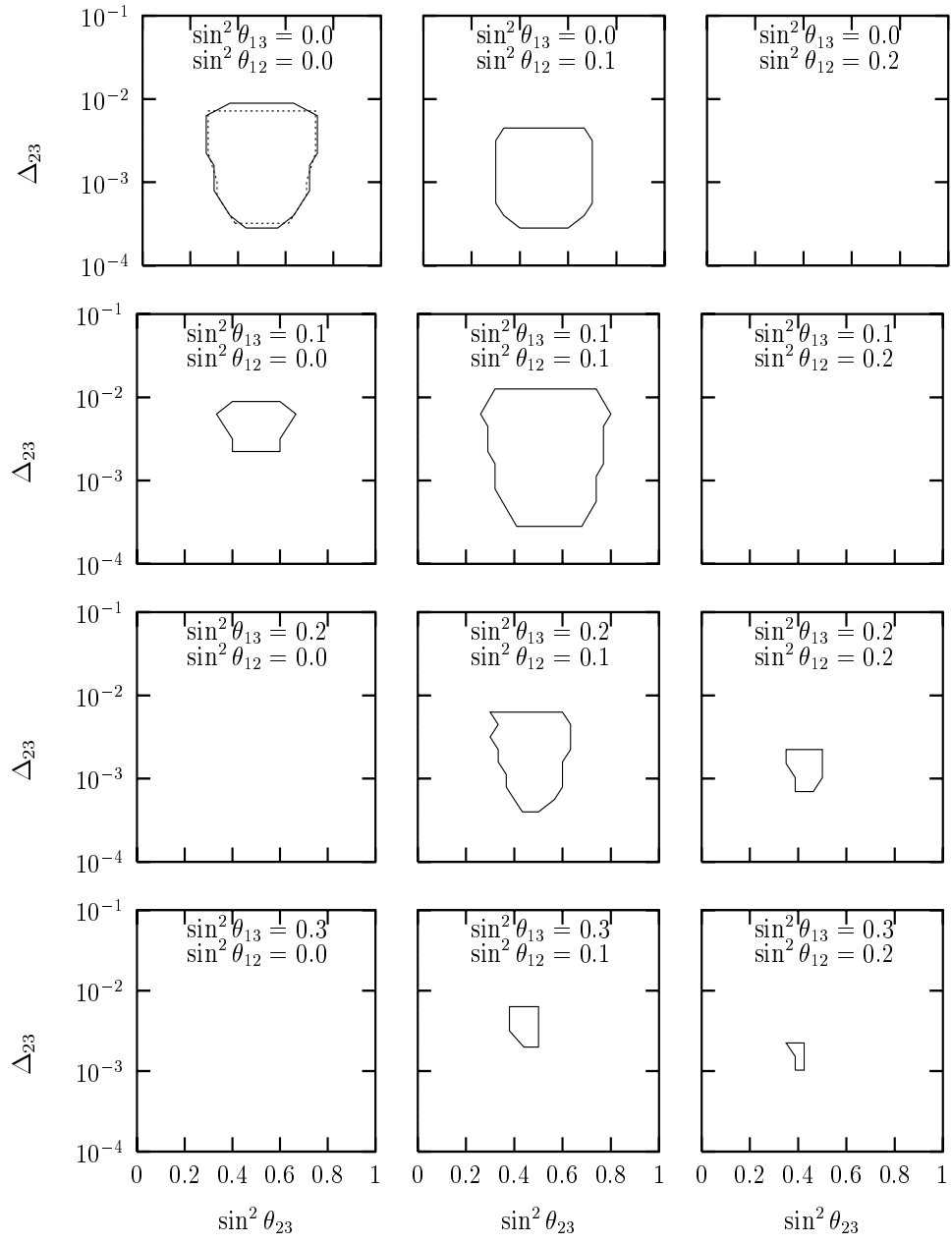


Fig. 4a

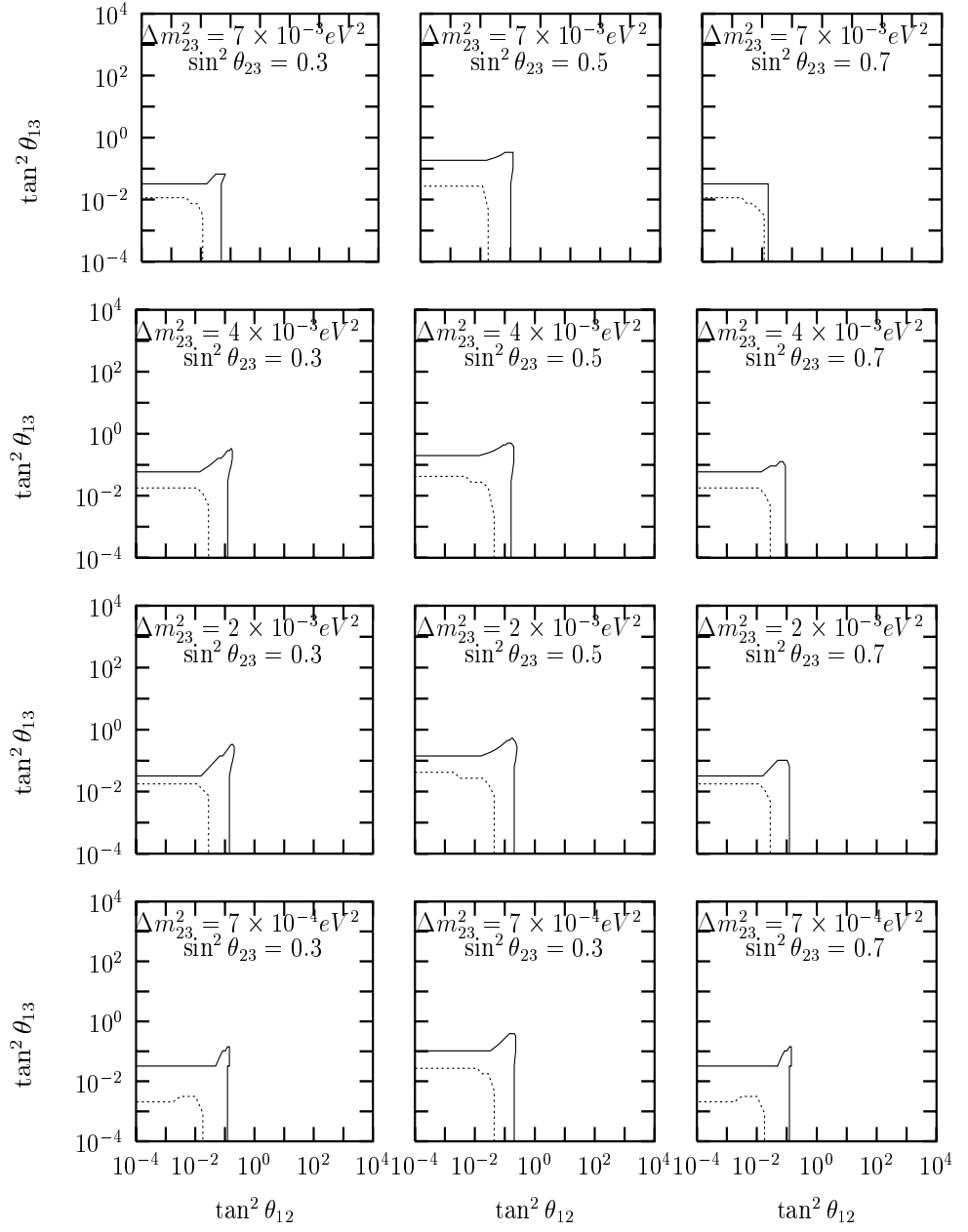


Fig. 4b

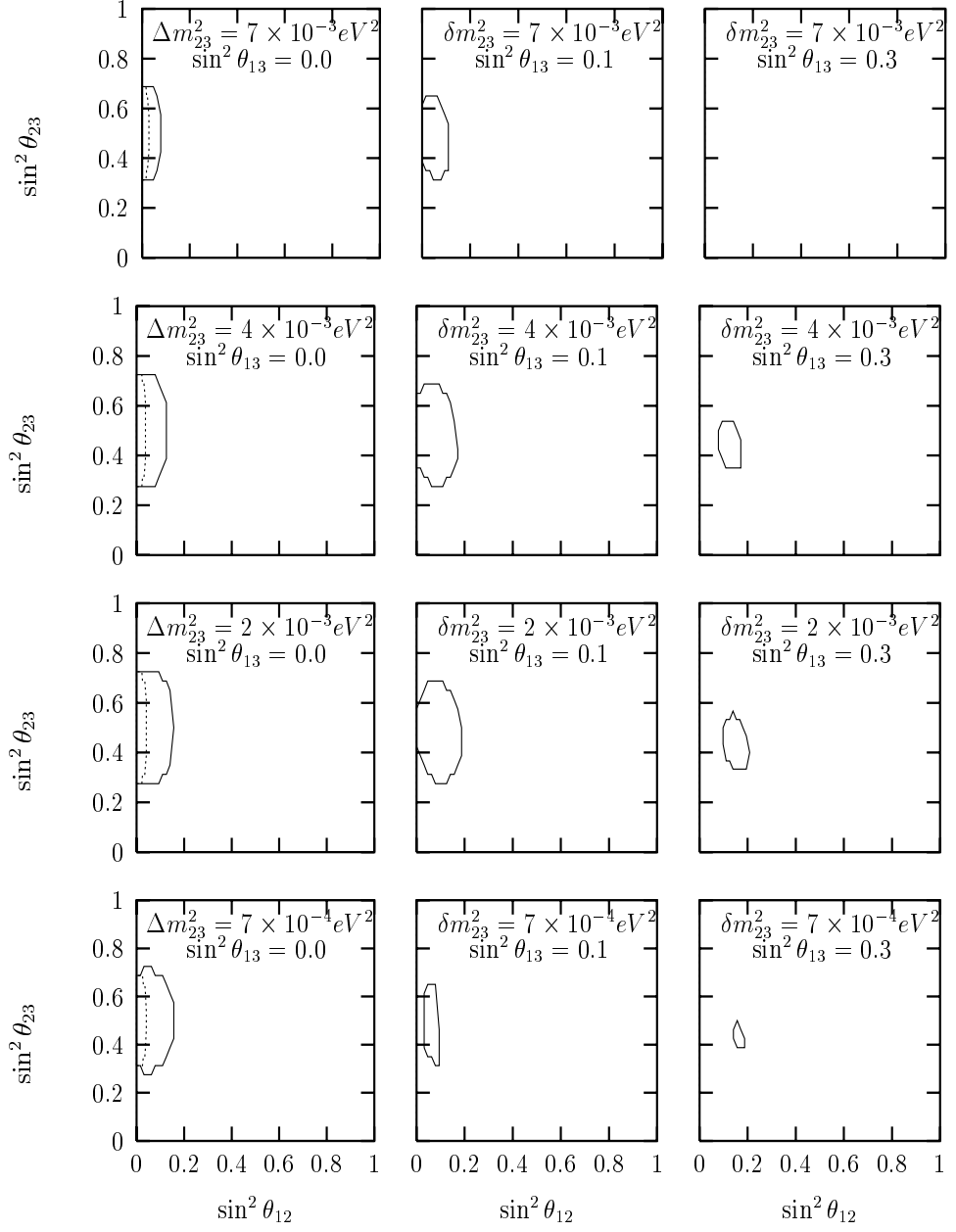


Fig. 4c

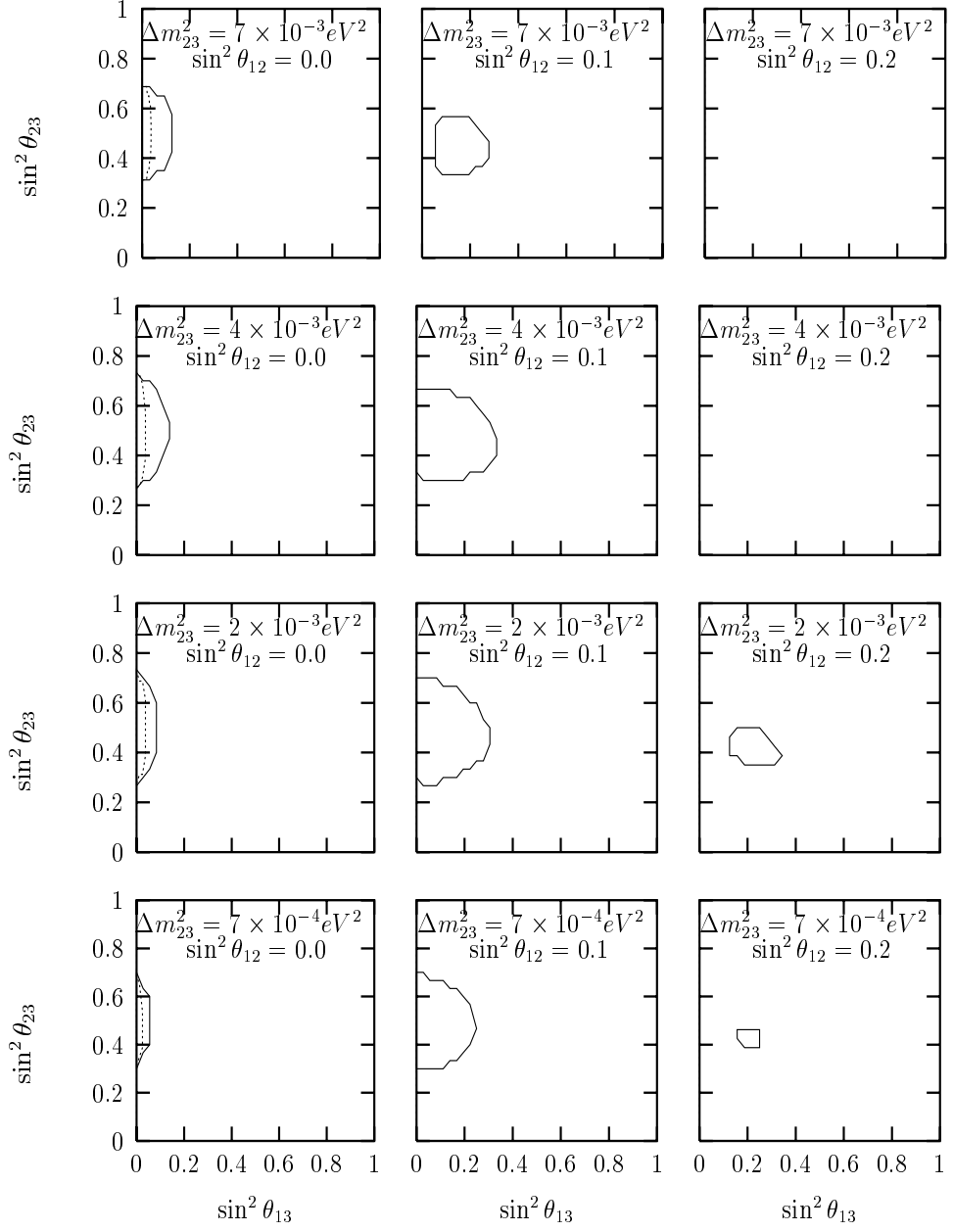


Fig. 4d

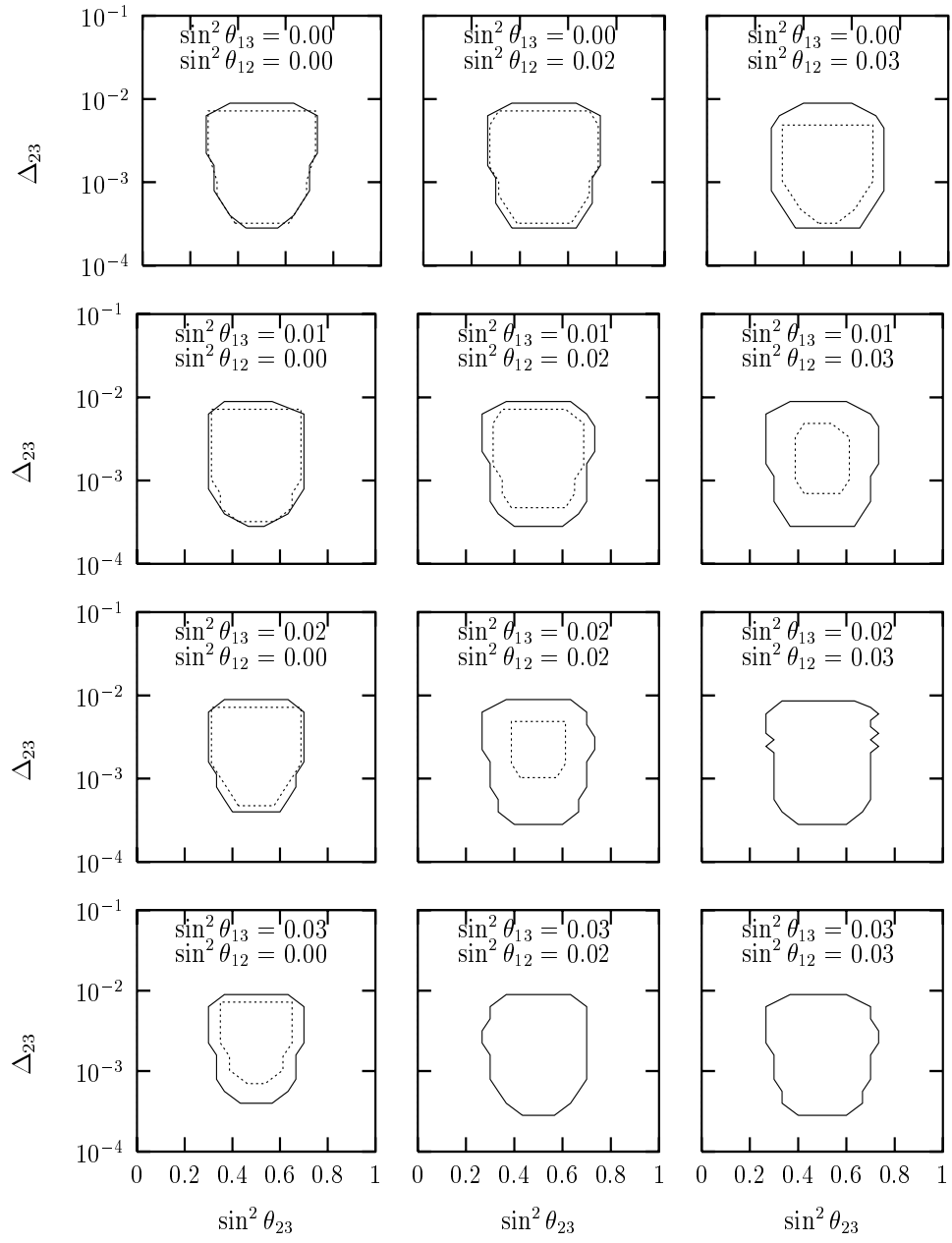


Fig. 5

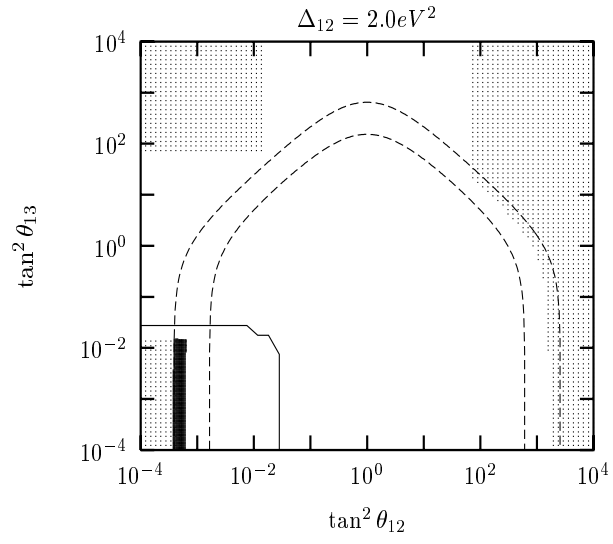
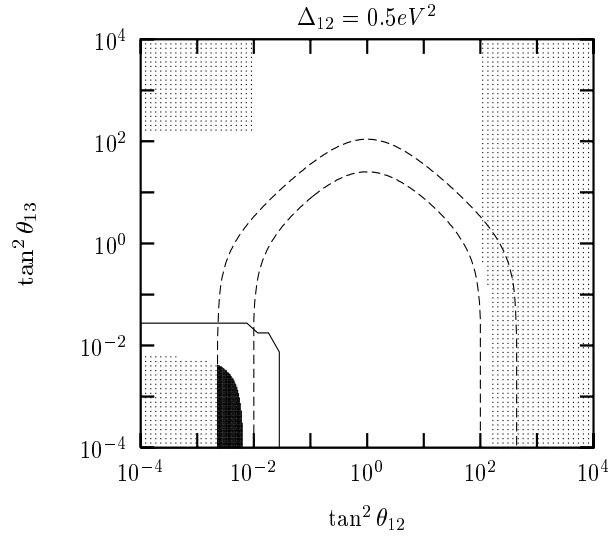


Fig. 6

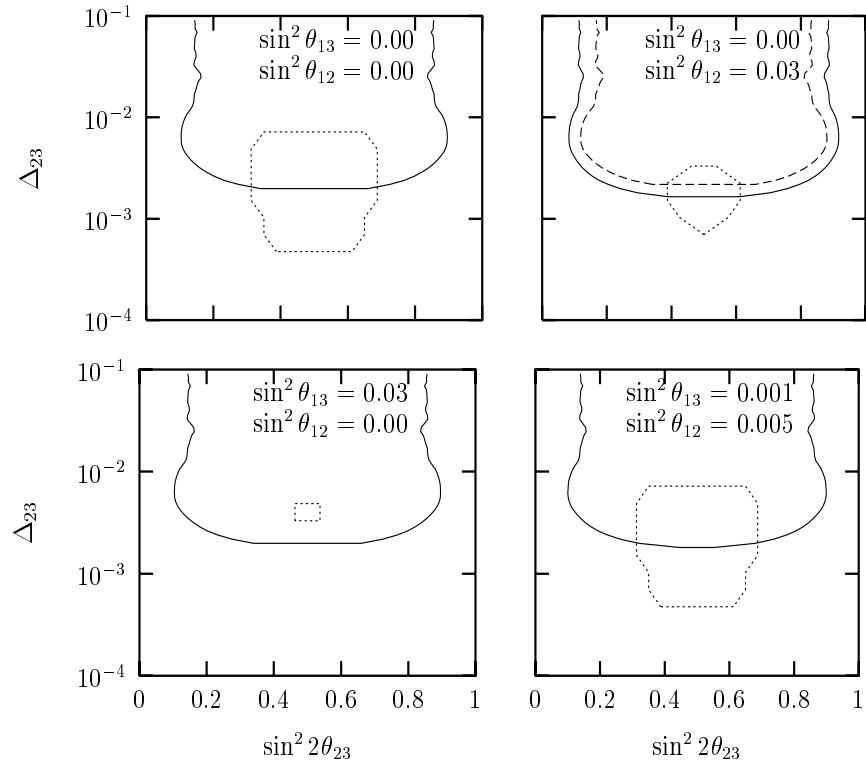


Fig. 7

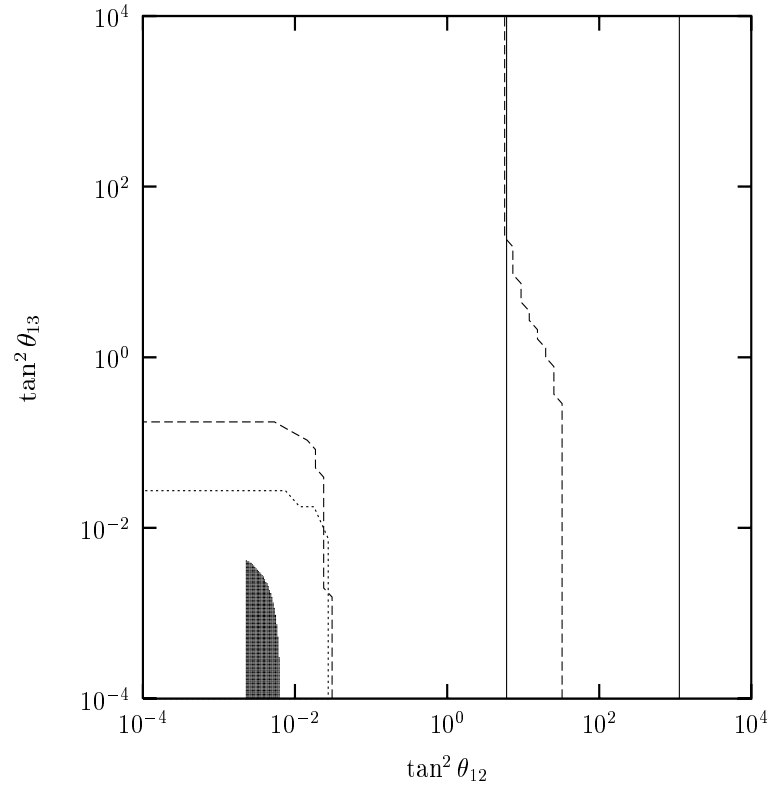


Fig. 8